IEEE Access
Multidisciplinary | Rapid Review | Open Access Journal

Received June 4, 2019, accepted June 17, 2019, date of publication June 20, 2019, date of current version July 15, 2019.

Digital Object Identifier 10.1109/ACCESS.2019.2924042

A Novel Stacked Denoising Autoencoder-Based Reconstruction Framework for Cerenkov Luminescence Tomography

XIN CAO[1,2], XIAO WEI[1,2], FENG YAN[1], LIN WANG[1,2], LINZHI SU[1], YUQING HOU[1,2], GUOHUA GENG[1], AND XIAOWEI HE[1,2]

[1]School of Information Science and Technology, Northwest University, Xi'an 710127, China
[2]Xi'an Key Laboratory of Radiomics and Intelligent Perception, Xi'an 710127, China

Corresponding author: Xiaowei He (hexw@nwu.edu.cn)

This work was supported in part by the National Natural Science Foundation of China under Grant 61701403, Grant 11571012, Grant 61806164, and Grant 61601363, in part by the Project funded by the China Post-Doctoral Science Foundation under Grant 2018M643719, Grant 2018M643717, and Grant 2019M653717, in part by the Young Talent Support Program of the Shaanxi Association for Science and Technology under Grant No.20190107, in part by the Postdoctoral Innovative Talents Support Program under Grant BX20180254, in part by the Scientific Research Program Funded by the Shaanxi Provincial Education Department under Grant 16JF026, Grant 17JF027, Grant 18JK0767, and Grant 18JK0778, in part by the Natural Science Research Plan Program in Shaanxi Province of China under Grant 2017JQ6017 and Grant 2017JQ6006, and in part by the Xi'an Science and Technology Project funded by the Xi'an Science and Technology Bureau under Grant 201805060ZD11CG44.

ABSTRACT Cerenkov luminescence tomography (CLT) is a promising imaging modality in the field of optical molecular imaging (OMI), which successfully bridges the OMI and tradition nuclear medical imaging and provides the location and quantitative analysis of the distribution of radionuclide probes inside the biological objects. As the CLT is an inherent highly ill-posed inverse problem, it is still a challenge to obtain an accurate reconstruction result. Here, we proposed a novel reconstruction framework based on stacking denoising autoencoders (SDAE), which serve as one famous structure of the artificial neural network (ANN). In our framework, the initial permission region is the whole domain and then a traditional reconstruction algorithm is used to reconstruct each node's energy. Then these nodes are clustered into two regions: permission region and non-permission region, and the permission region is used to start a new reconstruction loop where a new result can be obtained. The procedures above are repeated before the result meets the stop conditions. The numerical simulation experiments, physical phantom experiments and *in vivo* experiments are all carried out to validate the feasibility and potential of our framework. Results demonstrate that the proposed framework can indeed achieve a good performance in CLT reconstruction.

INDEX TERMS Cerenkov luminescence tomography, optical molecular imaging, reconstruction algorithm, stacking denoising autoencoders.

I. INTRODUCTION

Cerenkov Luminescence Imaging (CLI) is a new modality in the field of optical molecular imaging (OMI). Beyond the advantages of traditional OMI technologies, the attraction for many researchers is its wide availability in radionuclide which can be used for clinical studies approved by the Food and Drug Administration (FDA). Therefore, CLI can serve as the bridge between OMI and nuclear medical imaging [1]–[5]. The principle of CLI is that when charged particles (such as positrons) travel faster than light in the medium, spectrally continuous radiation (also named as Cerenkov Luminescence, CL) will be produced, known as Cerenkov Effect [6]. In 2009, Roberson et al. first applied CL to the field of OMI using 2-18fluoro-D-glucose (^{18}F-FDG), and named this new imaging concept as CLI [4]. Up to now, CLI has been successfully applied in the field of diagnostic imaging, drug development, intraoperative guidance, endoscopic imaging, and so on [7]–[20]. However, as CLI can only provide the two-dimension distribution of radionuclide probes, the lack of depth information restricts its further development, and the optical molecular tomography (OMT) [21] may provide a solution to conquer such limitation.

The associate editor coordinating the review of this manuscript and approving it for publication was Qiangqiang Yuan.

In 2010, Li et al. proposed a tomography method for CLI and named as Cerenkov Luminescence Tomography (CLT), which can reconstruct the three-dimension distribution of radionuclide probes inside biological object based several CLI images [22]. The emergence of CLT has enlarged the applicable area of CLI and soon become one of its research hot topics. Then, many researchers have proposed a variety of methods to improve the accuracy of CLT, as well as other OMT methods. For example, some of them use the location of CL source as the permission region to effectively improve the reconstruction accuracy [23]–[27]. The incorporation of the prior information has also been adopted in other OMT technologies, such as fluorescence molecular tomography and photoacoustic imaging [28], [29]. However, as a matter of fact, such a prior location of CL source cannot be obtained, while others use the whole domain for reconstruction directly [30]–[36]. As the permission region can improve the reconstruction result effectively, in 2016, Yu et al. proposed a method base on the Iteratively Shrinking Permission Region (ISPR) strategy for reconstruction, and in the method several loops of reconstruction are conducted. In each loop the permission region is the reconstruction result in its last loop. It demonstrates that the correct extraction of permission region is indeed a key point for achieving a good reconstruction result [37]. Different from the traditional RTE based methods mentioned above, the recent artificial neural network (ANN) may provide another solution to the OMT. Benefit from the rapid development of computer hardware technologies and the appearance of Big Data, the integration of ANN and medical imaging has become a hot topic and developed rapidly [38]–[41]. Gao et. al first applied the ANN to the field of OMT, proposing a novel machine-learning bioluminescence tomography (BLT) reconstruction strategy, which utilizes ANN to construct the inverse of the photon propagation directly by learning the nonlinear mapping relationship between the surface photon density and the bioluminescent source density [42]. Their result revealed that the proposed method can obtain a more accurate reconstruction result than those traditional reconstruction methods. However, the method limits its own availability due to its weak ability of generalization, i.e. a trained ANN can be only applied to a certain specified imaging object.

In this paper, we introduce ANN into CLT to propose a novel method for extraction of permission region and finally form a reconstruction framework for CLT [43]–[47]. It is worth noting that our framework is a loop structure, and that in each loop, the reconstruction region is clustered into the permission region and non-permission region. Here fuzzy C-means (FCM) [48]clustering algorithm is used. As it only includes the energy value, the original feature of one node in the reconstruction result will not serve as a sufficient input of FCM. By integrating one node's energy and its four neighborhood nodes' energies, we proposed a nearest four element fields (NFEF) strategy to extend the original feature of one node. We further obtain the latent features of the node, which may facilitate the clustering by using stacking denoising autoencoders (SDAE). Finally, we input the latent features of each node in FCM to obtain a correct permission region. The procedure above will be described in detail in Section 2.3. It should be noted that our framework can not only provide a relatively correct permission region but also significantly improve the quality of the recovered result which is commonly processed by setting manual thresholding to filter out the nodes with low energy values [49].

The rest of this paper is structured as follows. In Section II, the inverse problem of CLT, SDAE, NFEF theory and our reconstruction framework based on SDAE are represented. In Section III, we conduct the numerical simulation experiments and physical phantom experiments to demonstrate the effectiveness of our framework. Finally, we discuss the results and draw a conclusion in Section IV.

II. METHOD

A. RECONSTRUCTION PROBLEM

Usually, the Radiative Transfer Equation (RTE) is the best choice to describe the propagation of CL in biological tissues. However, its computational complexity is rather high [50]. According to the characteristics of low absorptivity and high scattering rate of photons in the process of biological tissue transmission, the simplified form of RTE, i.e. Diffusion Approximation (DA) model, has been developed to describe such a transmission procedure. The DA model combined with Robin's boundary conditions is described in Eq. (1) [37]:

$$\begin{cases} -\nabla \boldsymbol{D}(r)\nabla \boldsymbol{\Phi}(r) + \mu_{\boldsymbol{a}}(r)\boldsymbol{\Phi}(r) = \boldsymbol{S}(r), r \in \Omega \\ \boldsymbol{\Phi}(\xi) + 2\boldsymbol{FnD}(\xi) = 0, \xi \in \partial\Omega \end{cases} \tag{1}$$

where $\boldsymbol{\Phi}(r)$ denotes the photon flow rate at the point r in the region Ω, $\boldsymbol{D}(r) = 1/\left[3\left(\mu_a + \mu_s^{'}\right)\right]$ denotes the diffusion coefficient of the tissue, and μ_a and $\mu_s^{'}$ are the absorption coefficient and reduce scattering coefficient of tissue, respectively. The absorption coefficient and the reduced scattering coefficient are determined by the biological tissue itself. ξ denotes the point on the surface of the biological tissue, $\boldsymbol{F}$ is determined by the combination of the biological tissue and the refractive index of the air, and $\boldsymbol{n}$ is the unit normal vector whose direction is from the inside of the biological tissue to the outside of $\partial\Omega$. An adaptive *hp*-finite element method (*hp*-FEM) for bioluminescence source reconstruction proposed by our research group [51] is employed in this paper to recover the CL source distribution. Based on this algorithm, a linear relationship between the photon energy flow rate of the biological tissue surface and the unknown source distribution inside the tissue can be established:

$$\boldsymbol{AX} = \boldsymbol{B} \tag{2}$$

where $\boldsymbol{A}$ is the weight matrix, $\boldsymbol{B}$ is the photon flow rate measured at the boundary of the biological tissue, and $\boldsymbol{X}$ denotes the distribution of the unknown source within the desired biological tissue.

To solve the Eq. (2), here, we add L_1 regularization term to convert it into a minimization problem as Eq. (3):

$$\boldsymbol{X} = \underset{X \geq 0, X \in Permission\ region}{\operatorname{argmin}} \frac{1}{2} \|\boldsymbol{AX} - \boldsymbol{B}\|_2^2 + \tau \|\boldsymbol{X}\|_1 \quad (3)$$

where τ is the regularization parameter, which can be used to balance $\|\boldsymbol{AX} - \boldsymbol{B}\|_2^2$ and the regular penalty term $\|\boldsymbol{X}\|_1$.

B. AUTOENCODER, DAE AND SDAE

The autoencoder is a model capable of obtaining the feature representation of the given data [52]. Given a normalized input vector $\boldsymbol{x} = (x_1, x_2, , \ldots, x_N)^T$, the network first encodes it and generates a vector $\boldsymbol{y} = (y_1, y_2, \ldots, y_M)^T$, which is then used to be mapped back as a new vector $\boldsymbol{x}' = (x_1', x_2', \ldots, x_N')^T$, as shown in Eq. (4):

$$\begin{cases} \boldsymbol{y} = \sigma(\boldsymbol{W} * \boldsymbol{x} + \boldsymbol{b}) \\ \boldsymbol{x'} = \sigma(\boldsymbol{W}' * \boldsymbol{y} + \boldsymbol{b}') \end{cases} \quad (4)$$

where σ is the sigmoid function usually defined as $\sigma(t) = 1/(1 + e^{-t})$, $\boldsymbol{W}$ and $\boldsymbol{W'}$ are the weight matrices, and $\boldsymbol{b}$ and $\boldsymbol{b'}$ are the bias vectors. θ denotes the parameter set, i.e. $\theta = \{\boldsymbol{W}, \boldsymbol{W}^T, \boldsymbol{b}, \boldsymbol{b'}\}$. A loss function L is then established between $\boldsymbol{x}$ and $\boldsymbol{x}'$.Several forms can be used to establish L [52], and in this paper, the form of mean square error is employed, shown as Eq. (5):

$$L(\boldsymbol{x'}, \boldsymbol{x}) = \left\|\boldsymbol{x}' - \boldsymbol{x}\right\|^2 \quad (5)$$

By minimizing L, θ can be determined, and here the minimization problem is solved by the stochastic gradient descent algorithm, which can avoid the local minima of the training error [53]. In this way, $\boldsymbol{y}$ can be regarded as the latent feature of $\boldsymbol{x}$, and Fig. 1(a) shows a basic autoencoder intuitively.

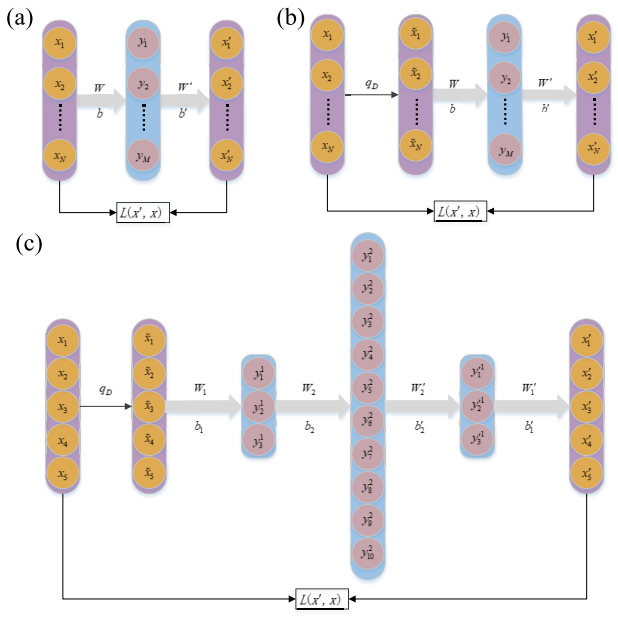

FIGURE 1. Illustrations of the basic AE (a) and DAE (b), while (c) depicts the structure of SDAE used in this paper.

To enhance the performance of AE, Vincent et al. used corrupted training data for input and achieve better learning accuracy, and called as denoising Autoencoder (DAE) [54]. In DAE, the input $\boldsymbol{x}$ is firstly corrupted as $\tilde{\boldsymbol{x}}$ by means of a stochastic mapping $\tilde{\boldsymbol{x}} \sim q_D(\tilde{\boldsymbol{x}}|\boldsymbol{x})$. As $\boldsymbol{x}'$ is the reconstruction of the corrupted data $\tilde{\boldsymbol{x}}$, the loss in the DAE model is measured by the reconstruction error L, which has the same form as Eq. (5), as shown in Fig. 1(b). In general, we can stack a number of DAEs to allow hierarchical feature extraction from input data, and this form is known as stacked denoising autoencoder (SDAE), as shown in Fig. 1(c). Different from AE or DAE, the shallow layer in the SDAE can represent the simpler patterns and the deep layer can learn a more complicated or abstract pattern inherent in the input data. In this paper, SDAE is used and the objective function is defined as:

$$J_{SDAE} = \frac{1}{m} \sum\nolimits_{t=1}^{m} L(\boldsymbol{x}^t, \boldsymbol{x'}^t) + \lambda \cdot \sum \|\omega\|_F \quad (6)$$

where m is the number of samples, t denotes the t-th AE in the SDAE, λ is a constant that balance the relative contributions of the reconstruction and the regularization terms, and ω is the set of weights in the network. For training the SDAE, a greedy layer-wise unsupervised learning algorithm is used, which has been proposed in [55]. After the training step, the deepest layer of the SDAE can produce the latent representation of the input, which will be used in our framework. It should be noted that the optimized method used in SDAE is also the stochastic gradient descent algorithm here.

C. SDAE BASED RECONSTRUCTION FRAMEWORK FOR CLT

The framework of the proposed SDAE based Cerenkov luminescence tomography is depicted in Fig. 2. It is easy to find out that our framework is an iterative process. Our framework contains two steps. First, we use the whole domain as the permission region to obtain the reconstruction result, and it is worth noting that the reconstruction algorithm is the incomplete variables truncated conjugate gradient, which has been proposed by our team in 2010 [56]. Then, SDAE is used to obtain the latent features of each reconstructed node's energy, and they are then used as the input of FCM to cluster the reconstructed nodes into two groups. The group with larger mean energy is chosen as the permission region in the iterative loop of two processes.

It should be noted that vector X denoted in Eq. (2) represents the energy of each node, which is the original feature of each node. Here, inspired by the applications of autoencoder in image-processing related studies [57], [58], we use each node's energy and tis four close nodes' energies as the extended original features, and we call this method as nearest Four Element Fields (NFEF). In NFEF strategy, the energy value of each node and the energy of its four nearest neighbors are combined, transforming the original result vector X in

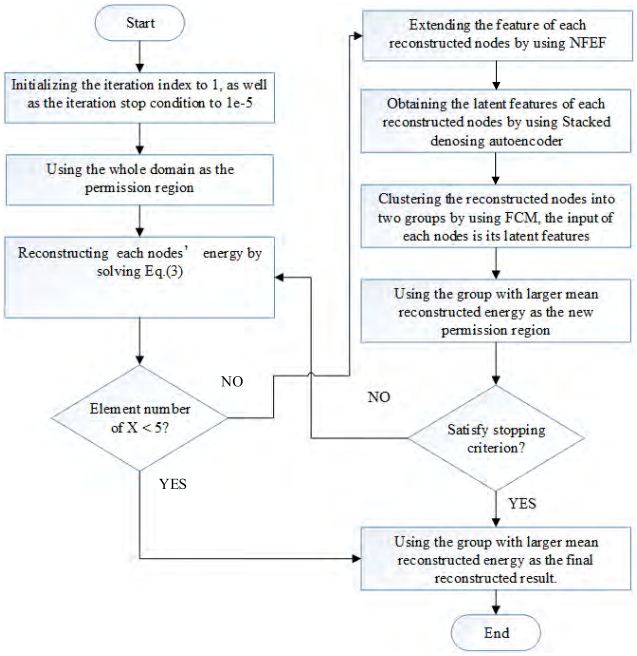

FIGURE 2. Framework of the proposed Cerenkov luminescence tomography method.

Eq. (2) to the following form:

$$M_{g\times 5} = \begin{bmatrix} x_1 & x_{N1,1} & x_{N1,2} & x_{N1,3} & x_{N1,4} \\ x_2 & x_{N2,1} & x_{N2,2} & x_{N2,3} & x_{N2,4} \\ \cdots & \cdots & \cdots & \cdots & \cdots \\ x_g & x_{Ng,1} & x_{Ng,2} & x_{Ng,3} & x_{Ng,4} \end{bmatrix} \quad (7)$$

where the first column of the $\boldsymbol{M}$ matrix is the original X vector, $x_{Ni,j}$ represents the j nearest neighbors of the ith element in the original X. Then, the matrix is regarded as the training data set to train SDAE. In addition, the number of the units of the input layer of SDAE in our framework is set as 5. Other parameters are set as: unit number of the layers are depicted in Fig. 1(c), and one dropout factor (probability = 40%) is used for the second hidden layer when training the network, aiming to reduce the overfitting problem of the network. The details of our proposed framework are summarized as follows:

III. EXPERIMENT AND RESULTS

In order to verify and systematically assess the performance and characteristics of the SDAE based CLT reconstruction framework proposed in this paper, four sets of numerical simulation experiments, two sets of physical experiments and one real implanted experiment are conducted. In all the experiments, the IVTCG algorithm and ISPR algorithm are used to compare the reconstruction results with our framework. In addition, to assess the stability, four levels of Gaussian noise experiments are also conducted in this section. The energy position error (E_L), reconstruction centroid error (E_{CoM}), reconstructed energy error (RE) and tetrahedral volume ratio (R_{TV}) are introduced as quantitative evaluation indicators.

Algorithm 1 SDAE Based Reconstruction Framework for CLT

Initialize. The global P_R as the initial feasible region, set the iteration index $z = 1$, the maximum iteration number $z_{max} = 20$, and the iteration stop condition $\beta = 1e-5$.
Step 1: Solve Eq. (3) by employing IVTCG reconstruction algorithm on the current permissible region and get a solution S_z, where z indicated that the current iteration index.
Step 2: Using NFEF to form a matrix $\boldsymbol{M}_z$ from S_z.
Step 3: For each row in $\boldsymbol{M}_z$, if the value of first column is 0, then delete it. If the rows of processed $\boldsymbol{M}_z$ is less than 5, then finish the loop and the S_z is final solution.
Step 4: Using $\boldsymbol{M}_z$ to train SDAE, then input $\boldsymbol{M}_z$ to encoder part of SDAE to generate a new matrix $\boldsymbol{M'}_z$ containing the features of each row in $\boldsymbol{M}_z$.
Step 5: For the set consists of the rows in $\boldsymbol{M'}_z$, using FCM algorithm to divide it into 2 subsets, the error threshold ξ of FCM is set to 1e-5, and the maximum number of iterations is set to 200.
Step 6: Calculating the mean energy value of the nodes corresponding to each subset, and the energy value of the nodes with smaller mean energy are set to 0, then a new solution, $S_z^{'}$ is obtained.
Step 7: Let $z = z + 1$. If $\left\|S_z - S_z^{'}\right\|_2 > \beta$, and $z < z_{max}$, let $S_z = S_z^{'}$ and repeat steps 3) to 7). Otherwise, $S_z{}'$ is the final solutions.

The energy position error E_L is defined as the Euclidean distance between the reconstruction point energy maximum point coordinates (x, y, z) and the real CL source coordinates (x_0, y_0, z_0):

$$E_L = \sqrt{(x - x_0)^2 + (y - y_0)^2 + (z - z_0)^2} \quad (8)$$

The reconstruction centroid error E_{CoM} is defined as the Euclidean distance between the centroid coordinates (x_g, y_g, z_g) of the reconstruction result and the centroid coordinates (x_{g0}, y_{g0}, z_{g0}) of the real CL source:

$$E_{CoM} = \sqrt{(x_g - x_{g0})^2 + (y_g - y_{g0})^2 + (z_g - z_{g0})^2} \quad (9)$$

The RE is defined as the relative error between the maximum reconstructed density and the actual one.

The tetrahedral volume ratio R_{TV} is defined as the ratio of the tetrahedral volume V_{ture} of the real CL source to the tetrahedral volume V_{rec} of the reconstruction result:

$$R_{TV} = V_{ture}/V_{rec} \quad (10)$$

The reconstruction accuracy is also quantified using the signal-to-noise ratio (SNR) and contrast-to-noise ratio (CNR), which can measure the visual quality, and how well features of interest are rendered by the reconstruction [59], [60]. The SNR is defined by

$$\text{SNR} = \frac{\sum_{i=1}^{n} x_i^2}{\sum_{i=1}^{n} (x_i - \tilde{x}_i)^2} \quad (11)$$

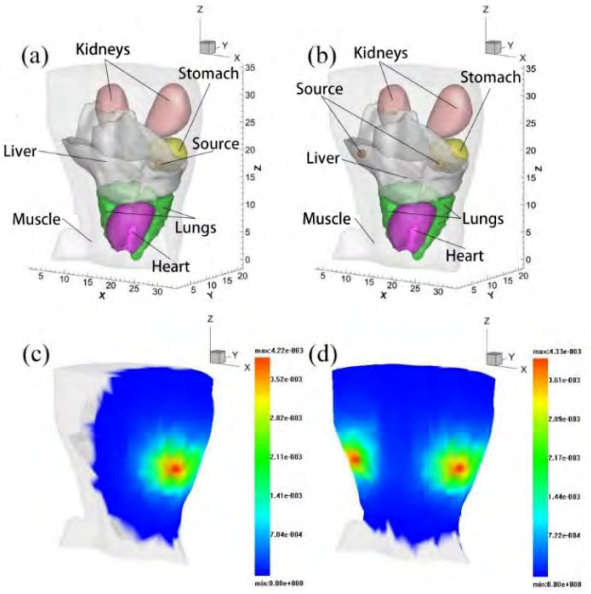

FIGURE 3. (a) Model of single source numerical mouse; (b) Model of double sources numerical mouse; (c) The forward simulation result of single source; (d) The forward simulation result of double source.

where $\tilde{x}_i$ denotes the energy of the i-th node in the reconstructed result, n denotes the total numer of the nodes in the numerical model, while x_i denotes the energy of the i-th node in the original numerical model. It should be noted that in the original numerical mode, the nodes' energies in the region of light source are all equal to 0.05.

We also defined the contrast-to-noise ratio (CNR) as:

$$\mathrm{CNR} = \frac{\mu_{ROI} - \mu_{BCK}}{\left(m_{ROI}\sigma_{ROI}^2 + m_{BCK}\sigma_{BCK}^2\right)^{1/2}} \tag{12}$$

where μ_{ROI} and μ_{BCK} are the mean values in the ROI and background, respectively, σ_{ROI}^2 and σ_{BCK}^2 are the variances, and m_{ROI} and m_{BCK} are the number of nodes included in the region of ROI and background, respectively. It should be noted that the region of ROI is where the light source is located, while that the region of background selected here is a region far away from the light source.

A. NUMERICAL MOUSE SIMULATION EXPERIMENT

The numerical mouse simulation experiment object is shown in Fig. 3, and the upper and lower portions thereof are inverted in all results. The numerical mouse contains five organs of heart, lung, liver, stomach, and kidney, and the rest is muscle tissue. The optical parameters of each organ and tissue are given in correlation researches [24], [61], as shown in Table 1. The forward model photon energy is generated by using Monte Carlo (MC) method, which is implemented by the Chinese Academy of Sciences Molecular Optical Simulation Environment (MOSE) software [62]. In a single light source experiment, a spherical light source with a radius of 0.8 *mm* and 0.05 nW/mm^3 power density is placed at coordinates (26 *mm*, 7 *mm*, 19 *mm*) as shown in Fig. 3(a). In the dual

TABLE 1. Optical parameters of different tissue and organs of the numerical mouse.

Material	μ_a / mm^{-1}	μ_s / mm^{-1}	g
Muscle	0.016	0.510	0.9
Heart	0.011	1.053	0.86
Stomach	0.002	1.525	0.9
Liver	0.065	0.723	0.9
Kidney	0.012	2.472	0.9
Lung	0.036	2.246	0.9

light source experiment, two spherical light sources with a radius of 0.8 mm and the same power density of 0.05 nW/mm^3 are posited at (26 *mm*, 7 *mm*, 19 *mm*) and (9 *mm*, 7 *mm*, 19 *mm*), as shown in Fig. 3(b). In both sets of experiments, the numerical mouse avatar is divided into 8858 nodes, 2206 surface elements, and 47407 internal tetrahedral finite element meshes. The numerical mouse forward simulation results are obtained through the MOSE software, shown in Figs. 3(c) and (d), followed by surface data reconstruction.

1) SINGLE SOURCE NUMERICAL MOUSE SIMULATION EXPERIMENT

Fig. 4 shows the reconstruction results of the three methods of IVTCG, ISPR, and our proposed framework in the case of single light source. It should be noted that for all these methods, the τ, which is important parameter of IVTCG, is a constant with the value of 0.04. The dark brown sphere represents the actual position of the Cherenkov fluorescence source, and the dark green region represents the reconstruction location of the light source. Figs. 4 (d), (e) and (f) are two-dimensional cross-sectional views of (a), (b) and (c) corresponding results

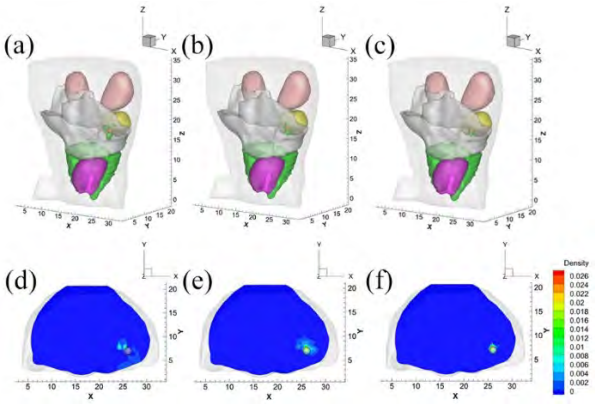

FIGURE 4. Reconstruction results of the single source numerical simulation experiment, (a)-(c) are stereograms of reconstruction results with IVTCG, ISPR and Our framework; (d)-(f) are cross-section views of the three methods at Z = 19mm, black circles show the real Cerenkov light sources.

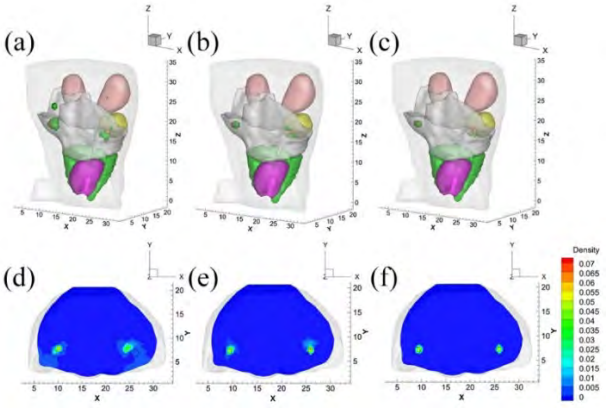

FIGURE 5. Reconstruction results of the double source numerical simulation experiment, (a)-(c) are stereograms of reconstruction results with IVTCG, ISPR and our framework; (d)-(f) are cross-section views of the three methods at $Z = 19$mm, and black circles show the real CL sources.

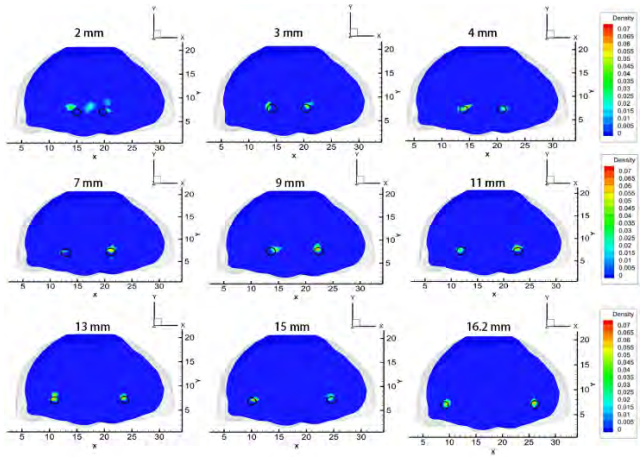

FIGURE 6. Axial slices ($Z = 19$mm) of the dual-source reconstructions with different edge-to-edge source distances, and the distance is labeled on the top of each images.

at $Z = 19$ mm, with black circles indicating the location of the real light source. The quantitative results are shown in Table 2. According to the experimental results, the ISPR reconstruction strategy can improve the reconstruction effect to a certain extent, but the feasible domain is still not accurate. Our framework can better construct a feasible domain based on energy distribution and spatial geometry information, resulting in a better reconstruction.

2) DOUBLE SOURCES NUMERICAL MOUSE SIMULATION EXPERIMENT

In order to demonstrate whether our framework has the ability to reconstruct multiple light sources, a double source simulation experiment is carried out in this part. Fig. 5 shows the reconstruction results of the three methods of IVTCG, ISPR and our framework in the case of double sources. The dark brown sphere represents the actual position of the CL source, and the dark green region represents the reconstruction location of the light source. Figs. 5 (d), (e) and (f) are two-dimensional cross-sectional views of (a), (b) and (c) corresponding results at Z = 19 mm, with black circles indicating the location of the real light source. The quantitative results are shown in Table 3, and it demonstrates that our framework can achieve a better reconstruction result than the other two methods.

In order to further investigate the reconstruction resolution of our framework. Eight dual-source numerical mice with different edge-to-edge source distances are designed. During the experiment, light sources are in different organs to make sure the result is robust. The reconstructed results are shown in Fig. 6, from which we can conclude that the minimum edge-to-edge, which can be distinguished from the reconstructed result by our framework, is in the range of (2mm, 3mm).

It can be seen from the two sets of experimental results of single and double light sources that compared with the IVTCG algorithm and ISPR algorithm, our reconstruction framework can significantly improve the reconstruction position accuracy under the same experiment settings. It can effectively reconstruct the result with the volume close to that of the real light source, instead of just reconstructing the correct coordinates and thus ignoring the geometric information of the light source. According to the definition of R_TV, the final reconstruction volumes of the IVTCG and ISPR algorithms are much larger than that of the real light source. It is worth noting that some methods which employ these two algorithms in the relevant literature often involves artificial threshold filtering to obtain a good visual effect, and that it is not needed in our framework.

3) NUMERICAL MOUSE NOISE EXPERIMENT

In order to verify the stability and reconstruction quality of our reconstruction framework under noise conditions, this paper designs a set of Gaussian noise experiments with four levels of 5%-20%. The quantitative results are displayed in Tables 4 and 5. At the four levels of 5%-20%, the E_L of single source and double source are 0.69-0.72 *mm* and 0.65-0.69 *mm*, respectively. The E_{CoM} are 0.53-0.69 *mm* and 0.65-0.86 *mm*, respectively. The R_{TV} are 1.25-1.30 and 1.16-1.22 respectively. Compared with the experiment with no additional noise, the reconstruction result is quite stable. Experiment results show that the Gaussian noise does not have a significant effect on our reconstruction framework, demonstrating the good stability and noise immunity of the proposed method.

B. PHYSICAL PHANTOM EXPERIMENT

1) MATERIALS AND INSTRUMENTS

In the phantom experiment, ^{18}F-deoxyglucose (^{18}F-FDG) is used as the radioactive material, and it was made by the *GE*'s Minitrace cyclotron. The radiochemical purity is 97%, and the radioactive concentration was 5GBq/mL, pH = 8.0, purity greater than 99.9%. Optical information was collected using an IVIS imaging system manufactured by Calipers Life Sciences, USA.

TABLE 2. Results of the three CLT reconstruction methods in single source numerical simulation.

Method	Actual source center/ *mm*	Reconstructed source center/ *mm*	Reconstructed source centroid center/ *mm*	E_L/ *mm*	E_{CoM}/ *mm*	R_{TV}	*RE*	SNR	CNR
IVTCG	(26,7,19)	(25.26,7.59,17.64)	(26.65,6.60,18.52)	1.65	0.90	0.33	30.61%	1.03	9.31
ISPR	(26,7,19)	(26.07,7.36,18.32)	(25.75,7.61,18.93)	0.77	0.66	0.56	27.33%	1.51	15.24
Our framework	(26,7,19)	(25.88,7.35,18.42)	(26.07,7.52,18.97)	0.69	0.53	1.25	24.72%	2.81	22.98

TABLE 3. Results of the three CLT reconstruction methods in double source numerical simulation levels.

Method	Actual source center/ *mm*	Reconstructed source center/ *mm*	Reconstructed source centroid center/ *mm*	Average E_L/ *mm*	Average E_{CoM}/ *mm*	Average R_{TV}	Average *RE*	SNR	CNR
IVTCG	(9,7,19)	(10.30,7.81,18.22)	(9.58,7.11,19.64)	1.93	1.11	0.35	28.67%	1.01	9.16
	(26,7,19)	(24.24,7.69,18.03)	(25.31,7.69,19.92)						
ISPR	(9,7,19)	(9.41,7.29,19.13)	(9.69,7.48,19.04)	1.22	1.04	0.72	23.91%	1.39	13.37
	(26,7,19)	(24.62,8.21,19.54)	(25.29,8.01,19.07)						
Our framework	(9,7,19)	(9.45,7.28,18.68)	(9.45,7.28,18.68)	0.65	0.65	1.16	18.62%	1.97	21.58
	(26,7,19)	(25.88,7.35,18.42)	(25.88,7.35,18.42)						

TABLE 4. Results of single source numerical simulation experiment under different noise levels.

Noise level/%	Actual source center/ *mm*	Reconstructed source center/ *mm*	Reconstructed source centroid center/ *mm*	E_L/ *mm*	E_{CoM}/ *mm*	R_{TV}	*RE*
5	(26,7,19)	(25.88,7.35,18.42)	(26.07,7.52,18.97)	**0.69**	**0.53**	**1.25**	**23.25%**
10	(26,7,19)	(25.88,7.35,18.42)	(26.07,7.52,18.97)	0.69	0.53	1.25	27.92%
15	(26,7,19)	(25.65,7.37,19.51)	(26.33,7.60,18.91)	0.72	0.69	1.30	25.56%
20	(26,7,19)	(25.65,7.37,19.51)	(26.33,7.60,18.91)	0.72	0.69	1.30	29.74%

TABLE 5. Results of double source numerical simulation experiment under different noise levels.

Noise level/%	Actual source center/ *mm*	Reconstructed source center/ *mm*	Reconstructed source centroid center/ *mm*	Average E_L/ *mm*	Average E_{CoM}/ *mm*	Average R_{TV}	Average *RE*
5	(9,7,19)	(9.45,7.28,18.68)	(9.45,7.28,18.68)	**0.65**	**0.65**	**1.16**	**19.49%**
	(26,7,19)	(25.88,7.35,18.42)	(25.88,7.35,18.42)				
10	(9,7,19)	(9.45,7.28,18.68)	(9.45,7.28,18.68)	0.65	0.74	1.16	23.85%
	(26,7,19)	(25.88,7.35,18.42)	(26.18,7.82,18,81)				
15	(9,7,19)	(9.45,7.28,18.68)	(9.45,7.28,18.68)	0.65	0.74	1.22	21.26%
	(26,7,19)	(25.88,7.35,18.42)	(26.18,7.82,18.81)				
20	(9,7,19)	(9.45,7.28,18.68)	(8.87,6.99,19.54)	0.69	0.86	1.22	23.47%
	(26,7,19)	(25.88,7.35,18.42)	(25.08,7.72,19.05)				

In this section, two sets of homogenous phantom experiments are designed. The phantom is made of polyformaldehyde and made into a cube whose side is 25 *mm* and a cylinder whose height and diameter are both 25 *mm* as well. A cylindrical hole is drilled from the top side of both phantoms, with the hole diameter of 3 *mm* and the depth of 12.5 *mm*. During the experiment, the 18F-FDG with a volume of about 10 μL is injected into the hole, forming a radionuclide cylinder with a height of about 2 mm. Moreover, the center coordinate is (6.25 mm, 0 mm, 1 mm), and a light-proof tape is used to seal the hole. The geometry of the phantoms with radionuclide cylinder is shown in Fig. 7. After the injection of radionuclide, the phantoms are placed into the IVIS system to acquire the CL signal transmitted from the surface of each phantom, and the obtained images are shown in Fig. 7(c) and (d).

TABLE 6. Results of the three CLT reconstruction methods in the cubic physical phantom experiment.

Method	Actual source center/ *mm*	Reconstructed source center/*mm*	Reconstructed source centroid center/ *mm*	E_L/ *mm*	E_{CoM}/ *mm*	R_{TV}
IVTCG	(6.25,0,1)	(4.34,-1.66,-0.03)	(4.95,0.86,0.65)	2.80	1.60	3.91
ISPR	(6.25,0,1)	(6.70,0.67,0.11)	(7.16,0.35,1.34)	1.20	1.03	1.65
Our framework	(6.25,0,1)	(5.76,-0.17,1.03)	(6.10,-0.17,1.37)	0.52	0.44	1.13

TABLE 7. Results of the three CLT reconstruction methods in the cylindrical physical phantom experiment.

Method	Actual source center/ *mm*	Reconstructed source center/ *mm*	Reconstructed source centroid center/ *mm*	E_L/ *mm*	E_{CoM}/ *mm*	R_{TV}
IVTCG	(6.25,0,1)	(5.13,-0.42,3.40)	(5.81,-0.41,-0.93)	2.68	2.02	2.94
ISPR	(6.25,0,1)	(5.18,-0.56,0.75)	(5.30,-0.44,0.71)	1.24	1.09	1.71
Our framework	(6.25,0,1)	(6.34,-0.32,1.05)	(6.34,-0.32,1.05)	0.34	0.34	1.14

TABLE 8. Results of the three CLT reconstruction methods in the real implanted experiments.

Method	Actual source center/ *mm*	Reconstructed source center/ *mm*	Reconstructed source centroid center/ *mm*	E_L/ *mm*	E_{CoM}/ *mm*	R_{TV}
IVTCG	(20.20,27.80,7.40)	(21.42,29.07,8.49)	(21.44,28.90,6.31)	2.07	1.98	4.62
ISPR	(20.20,27.80,7.40)	(20.37,29.19,8.61)	(21.21,28.73,6.07)	1.85	1.91	1.79
Our framework	(20.20,27.80,7.40)	(20.60,29.06,7.63)	(20.09,27.12,6.55)	1.34	1.09	1.57

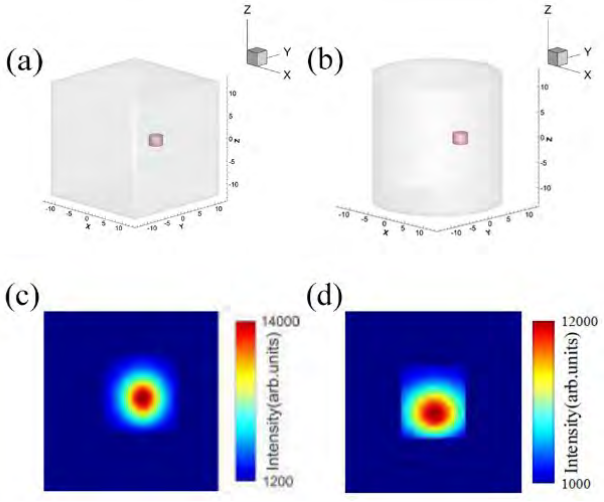

FIGURE 7. (a) and (b) are geometric structure of the cubic and cylindrical phantom with radionuclide injected; (c) and (d) are single-view collected of the two phantoms by IVIS system.

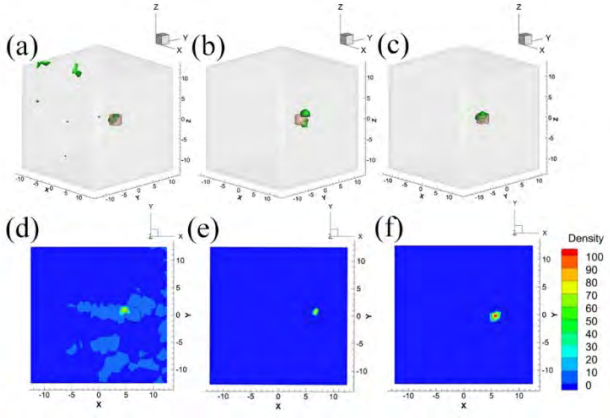

FIGURE 8. Reconstruction results of the cubic physical phantom experiment, (a)-(c) are stereograms of reconstruction results with IVTCG, ISPR and our framework; (d)-(f) are cross-section views of the three methods at $Z = 1mm$, and black circles show the real CL sources.

2) CUBIC PHANTOM EXPERIMENT

Figs. 8(a), (b) and (c) show the reconstruction results of the physical phantoms of the cube by the three methods: IVTCG, ISPR and our framework. The light pink cylinder indicates the actual position of the ^{18}F-FDG solution, and the dark green region indicates the reconstructed light source position. Figs. 8(d), (e) and (f) are two-dimensional cross-sectional views of (a), (b) and (c) corresponding results at $Z = 1$ mm, and black circles indicate the position of the real light source. The quantitative analysis of the results is shown in Table 6. It is obvious that the result of our framework is the best.

3) CYLINDER PHANTOM EXPERIMENT

Fig. 9(a), (b) and (c) show the reconstruction results of the cylinder phantom experiment. The light pink cylinder indicates the actual position of the ^{18}F-FDG solution, and the dark green region indicates the reconstruction light source position. Figs. 9(d), (e) and (f) are two-dimensional cross-sectional views of (a), (b) and (c) corresponding results at $Z = 1mm$, with black circles indicating the location of the real light source. The quantitative results are shown in Table 7. It can be concluded that our framework can achieve well reconstruction results in different geometrical morphologies.

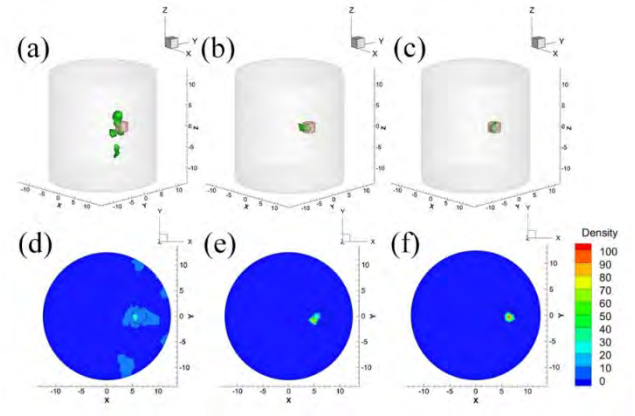

FIGURE 9. Reconstruction results of the cylindrical physical phantom experiment, (a)-(c) are stereograms of reconstruction results with IVTCG, ISPR and our framework; (d)-(f) are cross-section views of the three methods at $Z = 1mm$, and black circles show the real CL sources.

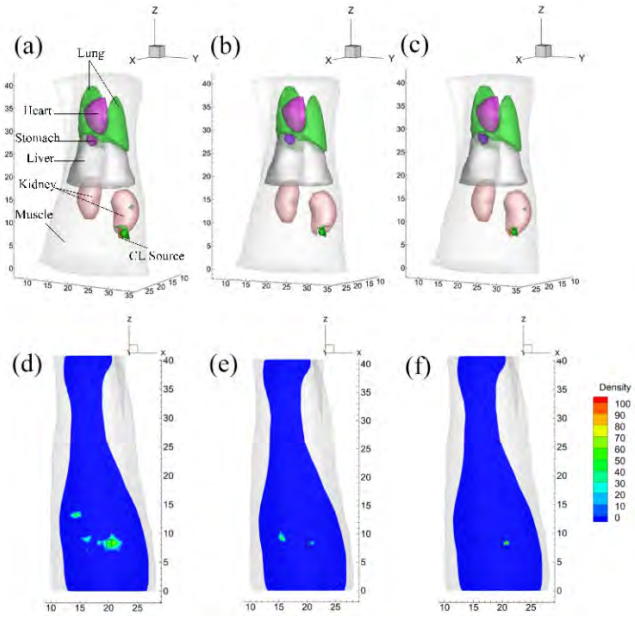

FIGURE 10. Reconstruction results of the real implanted animal experiment. (a)-(c) are stereograms of reconstruction results with IVTCG, ISPR and our framework; (d)-(f) are cross-section views of the three methods at $Y = 27.8mm$, black rectangle shows the real CL source.

C. REAL IMPLANTED ANIMAL EXPERIMENT

We further assess the performance of our proposed framework with implanted small animal experimental data. The experimental data were collected from the CLT/micro-CT dual-modal system on adult nude mice, and the mice were scanned with micro-CT. The torso section of the mice with a height of 41 mm is shown in Fig. 10(a). The main organs of the experimental mice include muscle, lung, heart stomach, liver, and kidney. The optical parameters of the organs are consistent with the literature [63]. We use an implanted 7.4 MBq of ^{18}F-FDG radioactive source to mimic the lesion contains radionuclide probe, and the location of the implanted source is (20.2 mm, 27.8 mm, 7.4 mm). Reconstruction results are shown in Figs. 10(c)-(e) and Table 8, which can demonstrate the ability of our proposed framework to recover the radionuclide distribution for *in vivo* experiments.

IV. DISCUSSION AND CONCLUSIONS

The combination of ANN and CLT (as well as the OMT) is a new research direction which may provide a more accurate reconstruction result than traditional OMT methods. However, how to implement such concept is a tough question. To our knowledge, only one attempt has been made by Gao et. al by applying multilayer perceptron to the field of OMT in 2018, which is of great significance in the development of OMT. However, their trained ANN can be only used to solve the inverse problem based on a specific object, resulting its relatively weak generalization ability, so this is the reason why we still use traditional mathematical method to solve CLT/OMT. In the field of classification, the ANN has found its successful application, while in the field of OMT, the permission region strategy can improve the reconstruction accuracy. Therefore, the incorporation of ANN to the extraction of permission region can serve as a feasible way to improve the reconstruction efficiency.

In this paper, we proposed a novel reconstruction framework for CLT. To test the performance of the reconstruction framework based on SDAE, simulation experiments, physical phantom experiments and in vivo animal experiments are conducted in this work. The IVTCG, ISPR are employed as compared reconstruction methods. The results demonstrate that our proposed method performs better than the two compared methods in both reconstruction accuracy and recovery visual effect. The main contributions of our work are: (1) using NFEF strategy to link neighborhood nodes together serving as the input of SDAE to extract latent features of each node; (2) using FCM to cluster the reconstructed nodes into two groups automatically and choosing the group with the large mean energy values as the permission region; (3) establishing a flexible framework, where many other reconstruction methods that may be more effective and efficient can also be integrated in the future.

As a summary, the framework proposed in this paper can improve the reconstruction accuracy effectively, and free from artificial intervention. We hope the proposed method can provide a useful tool for CLT, as well as other optical molecular tomography technologies.

REFERENCES

[1] M. A. Lewis, V. D. Kodibagkar, O. K. Öz, and R. P. Mason, "On the potential for molecular imaging with Cerenkov luminescence," *Opt. Lett.*, vol. 35, no. 23, pp. 3889–3891, 2010.

[2] Z. Hu, J. Liang, W. Yang, W. Fan, C. Li, X. Ma, X. Chen, X. Ma, X. Li, X. Qu, J. Wang, F. Cao, and J. Tian, "Experimental Cerenkov luminescence tomography of the mouse model with SPECT imaging validation," *Opt. Express*, vol. 18, no. 24, pp. 24441–24450, 2010.

[3] R. S. Dothager, R. J. Goiffon, E. Jackson, S. Harpstrite, and D. Piwnica-Worms, "Cerenkov radiation energy transfer (CRET) imaging: A novel method for optical imaging of PET isotopes in biological systems," *PLoS ONE*, vol. 5, no. 10, Oct. 2010, Art. no. e13300.

[4] R. Robertson, M. S. Germanos, C. Li, G. S. Mitchell, S. R. Cherry, and M. D. Silva, "Optical imaging of Cerenkov light generation from positron-emitting radiotracers," *Phys. Med. Biol.*, vol. 54, no. 16, p. N355, Jul. 2009.

[5] J. S. Cho, R. Taschereau, S. Olma, K. Liu, Y.-C. Chen, C. K.-F. Shen, R. M. van Dam, and A. F. Chatziioannou, "Cerenkov radiation imaging as a method for quantitative measurements of beta particles in a microfluidic chip," *Phys. Med. Biol.*, vol. 54, no. 22, p. 6757, Oct. 2009.

[6] J. Jelley, "Cerenkov radiation and its applications," *Brit. J. Appl. Phys.*, vol. 6, no. 7, p. 227, Jul. 1955.

[7] Y. Xu, H. Liu, and Z. Cheng, "Harnessing the power of radionuclides for optical imaging: Cerenkov luminescence imaging," *J. Nucl. Med.*, vol. 52, no. 12, pp. 2009–2018, Dec. 2011.

[8] R. Robertson, M. S. Germanos, M. G. Manfredi, P. G. Smith, and M. D. Silva, "Multimodal imaging with ^{18}F-FDG PET and Cerenkov luminescence imaging after MLN4924 treatment in a human lymphoma xenograft model," *J. Nucl. Med.*, vol. 52, no. 11, pp. 1764–1769, Nov. 2011.

[9] G. S. Mitchell, R. K. Gill, D. L. Boucher, C. Li, and S. R. Cherry, "*In vivo* Cerenkov luminescence imaging: A new tool for molecular imaging," *Philos. Trans. Roy. Soc. A, Math., Phys. Eng. Sci.*, vol. 369, no. 1955, pp. 4605–4619, Nov. 2011.

[10] G. Lucignani, "Čerenkov radioactive optical imaging: A promising new strategy," *Eur. J. Nucl. Med. Mol. Imag.*, vol. 38, no. 3, pp. 592–595, Mar. 2011.

[11] C. Q. Li, Y. Yang, G. S. Mitchell, and S. R. Cherry, "Simultaneous PET and multispectral 3-Dimensional fluorescence optical tomography imaging system," *J. Nucl. Med.*, vol. 52, no. 8, pp. 1268–1275, Aug. 2011.

[12] S. Y. Jeong, M.-H. Hwang, J. E. Kim, S. Kang, J. C. Park, J. Yoo, J.-H. Ha, S.-W. Lee, B.-C. Ahn, and J. Lee, "Combined Cerenkov luminescence and nuclear imaging of radioiodine in the thyroid gland and thyroid cancer cells expressing sodium iodide symporter: Initial feasibility study," *Endocrine J.*, vol. 58, no. 7, pp. 575–583, May 2011.

[13] J. P. Holland, G. Normand, A. Ruggiero, J. S. Lewis, and J. Grimm, "Intraoperative imaging of positron emission tomographic radiotracers using cerenkov luminescence emissions," *Mol. Imag.*, vol. 10, no. 3, p. 177, May 2011.

[14] F. Boschi, L. Calderan, and D. D'Ambrosio, M. Marengo, A. Fenzi, R. Calandrino, A. Sbarbati, and A. E. Spinelli, "*In vivo* ^{18}F-FDG tumour uptake measurements in small animals using Cerenkov radiation," *Eur. J. Nucl. Med. Mol. Imag.*, vol. 38, no. 1, pp. 120–127, Jan. 2011.

[15] A. E. Spinelli and D. D'Ambrosio, L. Calderan, M. Marengo, A. Sbarbati, and F. Boschi, "Cerenkov radiation allows *in vivo* optical imaging of positron emitting radiotracers," *Phys. Med. Biol.*, vol. 55, no. 2, p. 483, 2009.

[16] A. Ruggiero, J. P. Holland, J. S. Lewis, and J. Grimm, "Cerenkov luminescence imaging of medical isotopes," *J. Nucl. Med.*, vol. 51, no. 7, pp. 1123–1130, 2010.

[17] X. Cao, Y. H. Zhan, X. Cao, J. M. Liang, and X. L. Chen, "Harnessing the power of Cerenkov luminescence imaging for gastroenterology: Cerenkov luminescence endoscopy," *Current Med. Imag. Rev.*, vol. 13, no. 1, pp. 50–57, 2017.

[18] H. Hu, X. Cao, F. Kang, M. Wang, Y. Lin, M. Liu, S. Li, L. Yao, J. Liang, J. Liang, Y. Nie, X. Chen, J. Wang, and K. Wu, "Feasibility study of novel endoscopic Cerenkov luminescence imaging system in detecting and quantifying gastrointestinal disease: First human results," *Eur. Radiol.*, vol. 25, no. 6, pp. 1814–1822, Jun. 2015.

[19] X. Cao, X. Chen, F. Kang, X. Cao, Y. Zhan, J. Wang, K. Wu, and J. Liang, "Sensitivity improvement of Cerenkov luminescence endoscope with terbium doped Gd_2O_2S nanoparticles," *Appl. Phys. Lett.*, vol. 106, no. 21, May 2015, Art. no. 213702.

[20] X. Cao, X. Chen, F. Kang, Y. Zhan, X. Cao, J. Wang, J. Liang, and J. Tian, "Intensity enhanced Cerenkov luminescence imaging using terbium-doped Gd_2O_2S microparticles," *ACS Appl. Mater. Interfaces*, vol. 7, no. 22, pp. 11775–11782, Jun. 2015.

[21] S. R. Arridge, "Optical tomography in medical imaging," *Inverse Problems*, vol. 15, no. 2, p. R41, 1999.

[22] C. Li, G. S. Mitchell, and S. R. Cherry, "Cerenkov luminescence tomography for small-animal imaging," *Opt. Lett.*, vol. 35, no. 7, pp. 1109–1111, 2010.

[23] C. Wenxiang, W. Ge, K. Durairaj, L. Yi, J. Ming, W. V. Lihong, H. A. Eric, M. L. Geoffrey, M. C. Paul, Z. Joseph, and A. Cong, "Practical reconstruction method for bioluminescence tomography," *Opt. Express*, vol. 13, no. 18, pp. 6756–6771, 2005.

[24] M. A. Naser and M. S. Patterson, "Bioluminescence tomography using eigenvectors expansion and iterative solution for the optimized permissible source region," *Biomed. Opt. Express*, vol. 2, no. 11, pp. 3179–3193, Nov. 2011.

[25] M. A. Naser and M. S. Patterson, "Improved bioluminescence and fluorescence reconstruction algorithms using diffuse optical tomography, normalized data, and optimized selection of the permissible source region," *Biomed. Opt. Express*, vol. 2, no. 1, pp. 169–184, Jan. 2011.

[26] J. Feng, K. Jia, G. Yan, S. Zhu, C. Qin, Y. Lv, and J. Tian, "An optimal permissible source region strategy for multispectral bioluminescence tomography," *Opt. Express*, vol. 16, no. 20, pp. 15640–15654, Sep. 2008.

[27] A. E. Spinelli, C. Kuo, B. W. Rice, R. Calandrino, P. Marzola, A. Sbarbati, and F. Boschi, "Multispectral Cerenkov luminescence tomography for small animal optical imaging," *Opt. Express*, vol. 19, no. 13, pp. 12605–12618, Jun. 2011.

[28] S. Mandal, X. L. Deán-Ben, and D. Razansky, "Visual quality enhancement in optoacoustic tomography using active contour segmentation priors," *IEEE Trans. Med. Imag.*, vol. 35, no. 10, pp. 2209–2217, Oct. 2016.

[29] Y. Zhou, M. Chen, H. Su, and J. Luo, "Self-prior strategy for organ reconstruction in fluorescence molecular tomography," *Biomed. Opt. Express*, vol. 8, no. 10, pp. 4671–4686, Oct. 2017.

[30] Z. Hu, W. Yang, X. Ma, W. Ma, X. Qu, J. Liang, J. Wang, and J. Tian, "Cerenkov luminescence tomography of aminopeptidase N (APN/CD13) expression in mice bearing HT1080 tumors," *Mol. Imag.*, vol. 12, no. 3, pp. 173–181, 2013.

[31] Z. Hu, X. Ma, X. Qu, W. Yang, J. Liang, J. Wang, and J. Tian, "Three-dimensional noninvasive monitoring iodine-131 uptake in the thyroid using a modified Cerenkov luminescence tomography approach," *PloS OnE*, vol. 7, no. 5, May 2012, Art. no. e37623.

[32] Z. Hu, X. Chen, J. Liang, X. Qu, D. Chen, W. Yang, J. Wang, F. Cao, and J. Tian, "Single photon emission computed tomography-guided Cerenkov luminescence tomography," *J. Appl. Phys.*, vol. 112, no. 2, Jul. 2012, Art. no. 024703.

[33] J. Zhong, J. Tian, X. Yang, and C. Qin, "L_1-regularized Cerenkov luminescence tomography with a SP_3 method and CT fusion," in *Proc. Annu. Int. Conf. IEEE Eng. Med. Biol. Soc.*, Aug./Sep. 2011, pp. 6158–6161.

[34] J. Zhong, J. Tian, X. Yang, and C. Qin, "Whole-body Cerenkov luminescence tomography with the finite element SP_3 method," *Ann. Biomed. Eng.*, vol. 39, no. 6, pp. 1728–1735, 2011.

[35] K. Liu, Y. Lu, J. Tian, C. Qin, X. Yang, S. Zhu, X. Yang, Q. Gao, and D. Han, "Evaluation of the simplified spherical harmonics approximation in bioluminescence tomography through heterogeneous mouse models," *Opt. Express*, vol. 18, no. 20, pp. 20988–21002, Sep. 2010.

[36] J. Liu, Y. Wang, X. Qu, X. Li, X. Ma, R. Han, Z. Hu, X. Chen, D. Sun, R. Zhang, D. Chen, D. Chen, X. Chen, J. Liang, F. Cao, and J. Tian, "*In vivo* quantitative bioluminescence tomography using heterogeneous and homogeneous mouse models," *Opt. Express*, vol. 18, no. 12, pp. 13102–13113, Jun. 2010.

[37] J. Yu, B. Zhang, I. I. Iordachita, J. Reyes, Z. Lu, M. V. Brock, M. S. Patterson, J. W. Wong, and K. K.-H. Wang, "Systematic study of target localization for bioluminescence tomography guided radiation therapy," *Med. Phys.*, vol. 43, no. 5, pp. 2619–2629, May 2016.

[38] B. Zhu, J. Z. Liu, S. F. Cauley, B. R. Rosen, and M. S. Rosen, "Image reconstruction by domain-transform manifold learning," *Nature*, vol. 555, no. 7697, p. 487, 2018.

[39] A. Esteva, A. Robicquet, B. Ramsundar, V. Kuleshov, M. DePristo, K. Chou, C. Cui, G. Corrado, S. Thrun, and J. Dean, "A guide to deep learning in healthcare," *Nature Med.*, vol. 25, no. 1, pp. 24–29, Jan. 2019.

[40] J. He, S. L. Baxter, J. Xu, J. Xu, X. Zhou, and K. Zhang, "The practical implementation of artificial intelligence technologies in medicine," *Nature Med.*, vol. 25, no. 1, pp. 30–36, Jan. 2019.

[41] D. L. Thorek, A. Ogirala, B. J. Beattie, and J. Grimm, "Quantitative imaging of disease signatures through radioactive decay signal conversion," *Nature Med.*, vol. 19, no. 10, pp. 1345–1350, 2013.

[42] Y. Gao, K. Wang, Y. An, S. Jiang, H. Meng, and J. Tian, "Nonmodel-based bioluminescence tomography using a machine-learning reconstruction strategy," *Optica*, vol. 5, no. 11, pp. 1451–1454, Nov. 2018.

[43] Z. Hu, J. Tang, Z. Wang, K. Zhang, L. Zhang, and Q. Sun, "Deep learning for image-based cancer detection and diagnosis–A survey," *Pattern Recognit.*, vol. 83, pp. 134–149, Nov. 2018.

[44] S. De, D. Ratha, D. Ratha, A. Bhattacharya, and S. Chaudhuri, "Tensorization of multifrequency PolSAR data for classification using an autoencoder network," *IEEE Geosci. Remote Sens. Lett.*, vol. 15, no. 4, pp. 542–546, Apr. 2018.

[45] C. Lu, Z.-Y. Wang, W.-L. Qin, and J. Ma, "Fault diagnosis of rotary machinery components using a stacked denoising autoencoder-based health state identification," *Signal Process.*, vol. 130, pp. 377–388, Jan. 2017.
[46] K. G. Lore, A. Akintayo, and S. Sarkar, "LLNet: A deep autoencoder approach to natural low-light image enhancement," *Pattern Recognit.*, vol. 61, pp. 650–662, Jan. 2017.
[47] L. Su, M. Gong, P. Zhang, M. Zhang, J. Liu, and H. Yang, "Deep learning and mapping based ternary change detection for information unbalanced images," *Pattern Recognit.*, vol. 66, pp. 213–228, Jun. 2017.
[48] J. C. Bezdek, *Pattern Recognition with Fuzzy Objective Function Algorithms*. Springer, 2013.
[49] H. Yi, H. Wei, J. Peng, Y. Hou, and X. He, "Adaptive threshold method for recovered images of FMT," *J. Opt. Soc. Amer. A, Opt. Image Sci.*, vol. 35, no. 2, pp. 256–261, Feb. 2018.
[50] A. D. Klose, "The forward and inverse problem in tissue optics based on the radiative transfer equation: A brief review," *J. Quant. Spectrosc. Radiat. Transf.*, vol. 111, no. 11, pp. 1852–1853, Jul. 2010.
[51] R. Han, J. Liang, X. Qu, Y. Hou, N. Ren, J. Mao, and J. Tian, "A source reconstruction algorithm based on adaptive hp-FEM for bioluminescence tomography," *Opt. Express*, vol. 17, no. 17, pp. 14481–14494, Aug. 12009.
[52] P. Vincent, H. Larochelle, Y. Bengio, and P.-A. Manzagol, "Extracting and composing robust features with denoising autoencoders," in *Proc. 25th Int. Conf. Mach. Learn.*, Jul. 2008, pp. 1096–1103.
[53] J. Tang, C. Deng, G.-B. Huang, and B. Zhao, "Compressed-domain ship detection on spaceborne optical image using deep neural network and extreme learning machine," *IEEE Trans. Geosci. Remote Sens.*, vol. 53, no. 3, pp. 1174–1185, Mar. 2014.
[54] P. Vincent, H. Larochelle, I. Lajoie, Y. Bengio, and P.-A. Manzagol, "Stacked denoising autoencoders: Learning useful representations in a deep network with a local denoising criterion," *J. Mach. Learn. Res.*, vol. 11, no. 12, pp. 3371–3408, Dec. 2010.
[55] Y. Bengio, P. Lamblin, D. Popovici, and H. Larochelle, "Greedy layer-wise training of deep networks," in *Proc. 19th Int. Conf. Neural Inf. Process. Syst.*, Dec. 2006, pp. 153–160.
[56] X. He, J. Liang, X. Wang, J. Yu, X. Qu, X. Wang, Y. Hou, D. Chen, F. Liu, and J. Tian, "Sparse reconstruction for quantitative bioluminescence tomography based on the incomplete variables truncated conjugate gradient method," *Opt. Express*, vol. 18, no. 24, pp. 24825–24841, 2010.
[57] L. Su and X. Cao, "Fuzzy autoencoder for multiple change detection in remote sensing images," *Proc. SPIE*, vol. 12, no. 3, Aug. 2018, Art. no. 035014.
[58] S. Mei, Y. Wang, and G. Wen, "Automatic fabric defect detection with a multi-scale convolutional denoising autoencoder network model," *Sensors*, vol. 18, no. 4, p. 1064 Apr. 2018.
[59] J.-C. Baritaux, K. Hassler, M. Bucher, S. Sanyal, and M. Unser, "Sparsity-driven reconstruction for FDOT with anatomical priors," *IEEE Trans. Med. Imag.*, vol. 30, no. 5, pp. 1143–1153, May 2011.
[60] R. Malik, A. Kumpera, S. L. I. Olsson, P. A. Andrekson, and M. Karlsson, "Optical signal to noise ratio improvement through unbalanced noise beating in phase-sensitive parametric amplifiers," *Opt. Express*, vol. 22, no. 9, pp. 10477–10486, 2014.
[61] H. Guo, J. Yu, Z. Hu, H. Yi, Y. Hou, and X. He, "A hybrid clustering algorithm for multiple-source resolving in bioluminescence tomography," *J. Biophoton.*, vol. 11, no. 4, Apr. 2018, Art. no. e201700056.
[62] S. Ren, X. Chen, H. Wang, X. Qu, G. Wang, J. Liang, and J. Tian, "Molecular optical simulation environment (MOSE): A platform for the simulation of light propagation in turbid media," *PLoS ONE*, vol. 8, no. 4, Apr. 2013, Art. no. e61304.
[63] Y. Hungjian, C. Duofang, L. Wei, Z. Shouping, W. Xiaorui, L. Jimin, and T. Jie, "Reconstruction algorithms based on l1-norm and l2-norm for two imaging models of fluorescence molecular tomography: A comparative study," *Proc. SPIE*, vol. 18, no. 5, May 2013, Art. no. 056013.

XIN CAO received the B.S. degree in electronic engineering and the Ph.D. degree in pattern recognition and intelligent system from Xidian University, Xi'an, China, in 2011 and 2016, respectively.

Since 2016, he has been a Lecturer with the School of Information Science and Technology, Northwest University, Xi'an. He is currently a member of the Xi'an Key Laboratory of Radiomics and Intelligent Perception. His research interests include medical image analysis and optical molecular imaging.

XIAO WEI received the B.S. degree in physics from Northwest University, Xi'an, China, in 2016, where he is currently pursuing the M.S. degree in computer application technology.

He is currently a Student with the Xi'an Key Laboratory of Radiomics and Intelligent Perception. His current research interests include machine learning, deep learning, and their applications in medical image segmentation.

FENG YAN received the B.S. degree in software engineering from Northwest University, Xi'an, China, in 2018, where he is currently pursuing the M.S. degree.

His current research interests include image processing and intelligent information processing.

LIN WANG received the B.S. degree in electrical engineering and automation from Xidian University, Xi'an, China, in 2007, and the master's degree in pattern recognition and intelligent system from Xidian University. She is currently pursuing the Ph.D. degree in computer application technology with Northwest University, Xi'an. She is currently a Student with the Xi'an Key Laboratory of Radiomics and Intelligent Perception. Her current research interests include the development of system and algorithm in Cerenkov luminescence tomography and fluorescence molecular tomography.

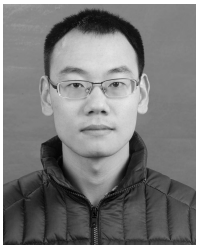

LINZHI SU received the B.S. degree in electronic engineering and the Ph.D. degree in circuits and systems from Xidian University, Xi'an, China, in 2011 and 2016, respectively.

Since 2016, he has been a Lecturer with the School of Information Science and Technology, Northwest University, Xi'an. His research interests include deep learning and computed tomography.

YUQING HOU received the B.S. degree from Northwest University, Xi'an, China, in 1984, and the M.S. degree from the Xi'an Institute of Optics and Precision Mechanics of CAS, Xi'an, in 1990.

She is currently a Professor with the School of Information Sciences and Technology, Northwest University. She is currently a member of the Xi'an Key Laboratory of Radiomics and Intelligent Perception. Her current research interests include digital image processing, big data in healthcare, and radiomics.

GUOHUA GENG received the Ph.D. degree in computer software and theory from Northwest University, Xi'an, China, in 2004, where she has been a Professor with the School of Information Science and Technology, since 2002. Her current research interests include computed tomography, medical image processing, parallel computing, and the digital restoration of cultural heritage.

XIAOWEI HE received the M.S. degree from the School of Electronic and Information Engineering, Xi'an Jiaotong University, Xi'an, China, in 2005, and the Ph.D. degree in pattern recognition and intelligent system from the School of Life Sciences and Technology, Xidian University, Xi'an, in 2011.

Since 2016, he has been a Professor with the School of Information Sciences and Technology, Northwest University, Xi'an. He is currently the Director of the Xi'an Key Laboratory of Radiomics and Intelligent Perception. His current research interests include medical imaging processing, 3D molecular imaging, and artificial intelligence.